Multidim Syst Sign Process (2012) 23:469–498
DOI 10.1007/s11045-012-0176-5

Contour extraction in medical images using initial boundary pixel selection and segmental contour following

Roy Chaoming Hsu · Din Yuen Chan · Cheng-Ting Liu · Wei-Chieh Lai

Received: 15 February 2011 / Revised: 22 December 2011 / Accepted: 9 January 2012 /
Published online: 22 February 2012

Abstract In today's health care, an imaging system plays an important role throughout the entire clinical process from diagnosis and treatment planning to surgical procedures and follow-up studies of disease. Boundary detection is a technique used to segment an object within a region of interest in the medical image for further clinical applications. Contour extraction is one of the most important boundary detection methods. In this paper, an object contour extraction for gray-level medical images using automatic initial boundary pixel selection and tracing of a segmental contour based on the boundary pixels obtained by the initial boundary pixel selection is proposed. Experimental results on artificial images of convex and deep concave objects, and real CT and MRI images show that, in comparing with other existing methods, a more detailed and accurate contour can be obtained using the proposed object contour extraction method. This has low computational complexity, which will benefit applications to clinical diagnosis, treatment, surgery, and follow up studies.

Keywords Boundary detection · Contour extraction · Snake · Medical imaging · ROI

1 Introduction

In medical images, the detection of object boundaries within a region of interest (ROI) can provide valuable information for diagnosis, treatment and other follow up studies of disease. Contour extraction is a classical boundary detection method regarded as a pre-processing for further image applications in medical images (Handels et al. 2010; Lehmann et al. 2004; Somkantha et al. 2010). Contour extraction methods could be categorized into edge-based

R. C. Hsu
Department of Electrical Engineering, National Chiayi University, 300 University Road, Chiayi City 600, Taiwan

D. Y. Chan (✉) · C.-T. Liu · W.-C. Lai
Department of Computer Science and Information Engineering, National Chiayi University, 300 University Road, Chiayi City 600, Taiwan
e-mail: dychan@mail.ncyu.edu.tw

(Canny 1986), region-based (Fu and Mui 1981), model-based (Kass et al. 1988), and tracing-based (Whithey et al. 2009; Chan and Hsu 2008). The edge-based method is the most commonly used boundary detection method. Recently, Suzuki et al. (2004) proposed an edge detector by combining with an artificial neural network for extracting left ventricular contours from left ventriculograms. Conventional edge-based methods detect the object's boundary efficiently using gradient operator, such as the Sobel operator (Gonzalez and Woods 2008), but closed contour results are not guaranteed which means these operators might not be very useful for applications in medical images. Region-based methods, on the other hand, set seed points in the image such that many objects can be classified according to homogeneous values around the seed points. An active contour model (Kass et al. 1988), a.k.a. snake, is a prominent model-based method for extracting object contours. Applications of snake have been widely used for extracting closed object contours in medical images (Pang et al. 2005; Yan and Kassim 2006). The snake extracts a closed contour using the idea of internal and external energy, where the internal energy smoothes the contour model and the external energy strengths contour model of the object. The most critical limitation in the conventional snake is that the initial boundary pixels, or snaxels, have to be selected around the object manually for increasing the accuracy and speed of convergence. Therefore, Xu and Prince (1998), and Sakalli et al. (2006) modified the external energy function to reduce convergence time and enhance extending the range of the traditional snake. However, most snake models are still very time consumption due to its computation complexity.

Tracing-based methods offer an alternative in constructing a closed contour in object boundary detection (Chen and Siy 1987; Chan and Hsu 2008; Banerjee et al. 2010). Chen and Siy (1987) proposed a contour tracing method by defining three stages which were edge detection, starting point parameter determination, and forward/backward boundary tracing. The first step of Chen and Siy's work is to detect edges of an object through the Sobel operator or other gradient operating mask. The second step finds the pixel as a starting point by a statistic method. Finally, the method traces the boundary with multi-directions from each starting point. In Chen and Siy's tracing method, certain conditions must be met to determine whether boundary tracing is finished or not and the direction of tracing is decided using gradient information. However, if convergence cannot be achieved in that direction, the tracing direction would be changed to the opposite to the original direction in searching for a closed contour. Hence, Chen and Siy's tracing method might fail to construct a closed contour if the image contains a large level of noise. Chan and Hsu (2008) presented a concise, robust shape-preserving contour tracing scheme for efficiently extracting a highly representative one pixel-width closed contour for the profiles of heterogeneous objects from digitally processed images regardless of noise existence. However, in developing the contour tracing scheme, the fundamental assumption is made that the object pixels have already been separated from the background pixels via some ordinary image segmentation processing, where a thresholding technique (Otsu 1979) is usually adopted. In other words, the contour tracing scheme is designed for processing the images within which heterogeneous objects have already been distinguished from each other. Recently, Banerjee et al. (2010) proposed a contour following method for tracing an object's boundary. The method selected the maximum gradient value of three search directions as contour point; the search directions can be increased to 5 or 7 whenever required.

Besides contour extraction, *graph cut*-based minimization for boundary and region segmentation of objects (Boykov and Jolly 2011; Rother et al. 2004) won a lot of popularity for its applications in image and video editing. The key idea of graph cut is the flexible definition of widely extracted low-level cues for similarity comparisons in the pixels clustering according to various applications. One cue of the most significant is the color feature

to support the pixel-based color image segmentation. Yet, relatively, when the portion of exterior object having close colors to that of its near target object, which the user would like to segment, the common graph cut processing will possibly mistake the marginal portion of target object as the part of background. For handling this problem, Lempitsky et al. (2009) create a special middle box within the user-provided bounding box and the short and long crossing path is defined inside the middle box and the bounding box, respectively, for introducing the tightness. And then, when the cost (energy) function associated with neighboring pixels is minimized for performing the judgment of pixel-attribute being either background or foreground, the proposed tightness prior for path connection is added as given constraints into the graph cut framework. The proposed image segmentation with a bounding box prior, henceforth abbreviated as ISBBR, is viewed as the improved pixel-based graph-cut solution with realization of merging a tightness-prior opinion. Basically, it can indeed offer very impressing performance for color image segmentation. Although, the proposed "pinpointing" procedure is guaranteed to have the polynomial-time complexity via relaxing the integrality constraints of theoretical graph cut, the high time consuming is still inevitable and it needs the aid of prior information about foreground pixels in so-called crossing paths. Besides, when the inner of user-made bounding box is automatically generated with an unsuited (mistaken) middle box, more false-positives (or even false-negatives) may be caused over traditional graph-cut algorithm in semantic segmentation.

Certain contour extraction methods often are executed interactively with its users, such as the snake, however, the methods are very time consuming due to the human-machine interaction when large amounts of image data, such as medical images, are being processed and they are subject to operator's variability as well. Therefore, in performing contour extraction for medical images, automatic or semi-automatic methods in reducing laborious manual work, such as conventional snaxel initialization in active contour model, are preferred. In an image analysis environment, such as medical images with background noise, automatic initialization of boundary pixels for contour extracting using a simple algorithm is very difficult. Recently, methods on automatic initialization of boundary pixels were proposed (Yuen et al. 1999; Chuang and Lie 2001; Dang et al. 2009; Chan et al. 2009; Delmas et al. 1999; Bakir and Charfi 2009; Teixeira et al. 2008). Yuen et al. (1999) proposed an initial snaxel selection method to search initial snaxels around the object, and an energy function to solve the concave problem and detect multiple objects. The first step of Yuen's method is to emit straight lines from the center of gravity, with equivalent angles between each pair of straight lines. For each straight line, the gradient values of pixels is computed and used to determine the suitable snaxels whose gradient value should be greater than a threshold value. When an initialized snaxel cannot be found, the center of gravity will be selected as the initial snaxel which implies that the image can have multiple objects. Therefore, the initialization snaxels are classified to different objects and an active contour model is used for tracing multiple objects. The snaxel initialization of Yuen et al. can efficiently select initial snaxels; however, the automatic initialization method is designed for an active contour model, which will suffer from the problem of intensive computational complexity.

In this study, a contour extraction method is proposed for object boundary detection in gray-level medical images. The proposed method of contour extraction in medical images comprises two discrete but consecutively integrated mechanisms, namely the initial boundary pixel selection (IBPS) and the segmental contour following (SCF) (Hsu et al. 2010b). The IBPS is basically designed to first automatically find the skeleton of an object and determine the object's morphological geographic center (OMGC). The IBPS searches the scan-lines emitting from the OMGC through the end-points of the object skeleton for the initial boundary pixels. These new scan-lines are constructed between each pair of neighboring initial

boundary pixels. The IBPS then successively selects a new initial boundary pixel along each new constructed scan-line so as to form a set of initial boundary pixels of the object profile. Following the IBPS, the SCF traces the object contour using the relative direction and gravitation of gradient (GoG) between any two neighboring initial boundary pixels selected by IBPS to finally construct a closed contour of the object. The consecutively integrated IBPS-SCF contour extraction method, designated as ISCEM hereafter, is designed to extract a closed contour of an entire object contour from the region of interest (ROI) of a noisy medical image. Contributions of the ISCEM are the following

1. The IBPS extends the initial snaxel selection method (ISSM) of our earlier work (Hsu et al. 2010a) for an object with deep concavities, such as a U-shape, by integrating the processes of skeletonization and OMGC search with much improved accuracy in locating initial boundary pixels for an object.
2. With a few modifications in the IBPS, the ISCEM is extended for contour extraction of multiple objects without changing the essentiality of structure.
3. Moreover, the IBPS is independent of boundary extraction methods, hence; IBPS also could be applied to handle the snaxel initialization problem in an active contour model, i.e., snake, or other contour following methods such as SCF.
4. Besides, the SCF traces the segmented contour between each pair of neighboring initial boundary pixels and it is particularly suitable for parallel processing when large amounts of medical imaging data are to be processed simultaneously.

By incorporating the SCF with the IBPS extension, the ISCEM presents a simple but effective boundary extraction method which delineates the contour of multiple objects with details and high precision. Yet it requires much less computational time when compared to a snake.

2 The proposed method

Figure 1 presents the process flow diagram of the ISCEM showing the steps of ROI selection, IBPS and SCF. In brief, a region of interest (ROI) from a medical image is first selected by the user. The IBPS then divides an object's contour into contour segments by finding boundary pixels on scan-lines emitting from the OMGC and going through the end points of the object skeleton. Following the IBPS, the SCF efficiently decides contour points with lower computational effort using relative direction and gravitation of gradient between the source and target boundary pixels.

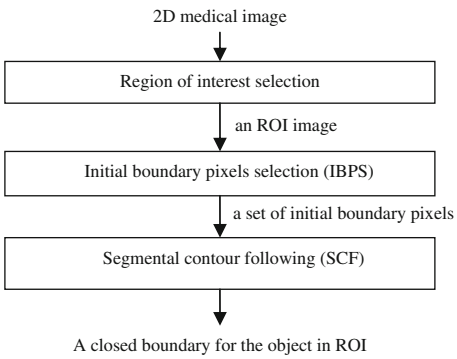

Fig. 1 The process flow diagram of the proposed ISCEM

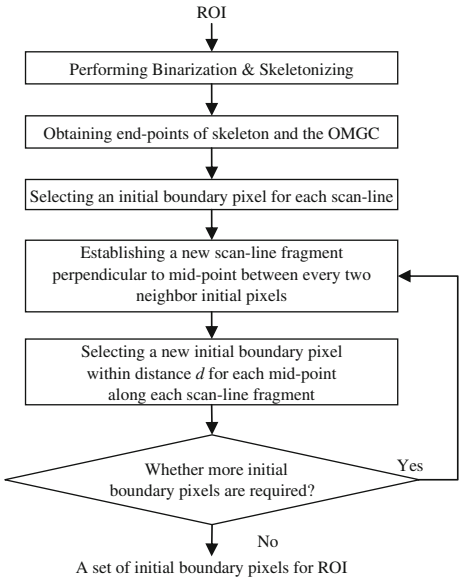

Fig. 2 The detailed processing steps of IBPS

The user interaction of ROI selecting is similar to the bounding box interaction in the ISBBR (Lempitsky et al. 2009); however, the bounding box in ISBBR is to obtain the tightness prior in improving the graph-cut algorithm for segmentation of error-prone portions in complicated color images. On the contrary, ROI selection in our ISCEM is simply employed in restricting the attention of the image segmentation process to the interior of the ROI, which mechanism provides high application preference in extracting object contour of gray-level images especially for medical ones. In our approach, the rectangle initial mask, i.e., ROI, provided by user needs not be too strict for an adequate tightness to the target object border for most cases. Rather, our proposed ISCEM is a concise yet robust integrated edge- and tracing-based mechanism, i.e., IBPS and SCF, respectively. In effect, our algorithm is considerably simpler than the original prototype graph-cut approach and the ISBBR as well. In summary, from the aspect of initialization significance in robustness, the ISBBR particularly considers the employment of tightness prior to the graph-cut approach for pursuing more robustness against the misleading of background close to the target object. Hence, the segmentation performance of ISBBR is quite associated with the appropriation of making user-provided bounding box and the middle box. Relatively, the creation of initial user-defined rectangle in the proposed ISCEM need not be precise or cautious in comparing to that in the algorithm in ISBBR and the robustness is substantially inherent in the structure of our proposed ISCEM, which effectively and consecutively incorporates "skeleton" and "divide-and-conquer" processes.

2.1 Initial boundary pixel selection (IBPS)

The detailed processing steps of the IPBS are illustrated in Figure 2. The IBPS process commences by selecting a ROI containing a salient object from a medical image. Considering the task of object contour extraction from the ROI of a medical image, the object of most interest is located at the center of the ROI such that the position of the center of gravity (CoG) is often located around the center of the object (Hsu et al. 2010a). However, for an object

with irregular or deep shape of concavities the CoG might be outside the body of the object and the ISSM of our previous work (Hsu et al. 2010a), which searches for initial boundary pixels along the scan-lines emitting from the CoG, might locate some false initial boundary pixels. Hence, different to the ISSM, the IBPS finds the skeleton of the object from the ROI, determines the OMGC from the skeleton, and searches for the initial boundary pixels on the object contour along the initial scan-lines radiating from the OMGC to the end points of object's skeleton. Once a ROI image, containing an interested object to be analyzed, is selected from a medical image, the binarization (Otsu 1979) and skeletonizing (Guo and Hall 1989) are performed on the ROI image to obtain the object's skeleton, represented as a set of skeleton pixels, S_n, as the following

$$S_n = \{(x_i, y_i) | \forall (x_i, y_i) \in \text{skeleton pixels of an object}, i = 1, \ldots, n\} \tag{1}$$

The object's skeleton is a good morphological representation of the object's shape in the ROI image. The end points of an object's skeleton e, is a subset of S_n and is represented as

$$e = \{(x_i, y_i) | \forall (x_i, y_i) \in \text{end points of an object keleton}, i = 1, \ldots, t\} \tag{2}$$

where the end points in e are obtained by identifying these points in the S_n with their 8-neighbors having only one point in the S_n. The position of the approximate OMGC, c, can now be obtained from the end points in the S_n by

$$c = \left\{ (x_c, y_c) | x_c = \frac{\sum_{i=1}^{t} x_{e,i}}{t}, y_c = \frac{\sum_{i=1}^{t} y_{e,i}}{t}, (x_{e,i}, y_{e,i}) \in e, i = 1, \ldots, t \right\} \tag{3}$$

where $x_{e,i}$ and $y_{e,i}$, respectively, are the coordinates of the end points in the x and y directions, and t is the total number of end points of the object's skeleton. A refined OMGC search is used to locate the final OMGC iteratively according to the following

$$\begin{cases} \text{OMGC}\,(x, y) = c, & \text{if} \quad c \in S_n \\ c \text{ is considered as a base point, } b_i, & \text{otherwise} \end{cases} \tag{4}$$

where the base point b_i is defined as the starting point for searching the final OMGC. If $c \notin S_n$, three scenarios are considered, as shown in Fig. 3, in obtaining the final OMGC by scanning along the x and y directions from the position of c for locating the point(s) on the skeleton. Assuming that the located skeleton points along the x and y direction, respectively, are $b_{x,i}, i = 0, 1, \ldots, n$, and $b_{y,j}, j = 0, 1, 2 \ldots, m$, where n and m, respectively, is the number of located skeleton points on the x and y directions and the total number of located skeleton points is $n + m = p$. Three scenarios for reaching the final OMGC are the following

1. $p = 2$ and $n = m = 1$, as shown in Fig. 3a. If the bx_x and by_y, respectively, are the x and y coordinates of $b_{x,1}$, and $b_{y,1}$, the final position of OMGC is

$$\text{OMGC} = (bx_x, by_y) \tag{5}$$

2. $p = 3$ and either $n = 1$ or $m = 1$, as shown in Fig. 3b. The located skeleton point with n=1 or m= 1 is selected as the final OMGC, i.e.,

$$\text{OMGC} = \begin{cases} b_{x,n}, & \text{if} \quad n = 1 \\ \text{b}_{\text{y,m}} & \text{else} \quad \text{if}\, m = 1 \end{cases} \tag{6}$$

3. $p = 4$ and $n = m = 2$, as shown in Fig. 3c. The base point b_i is regarded as the final MOGC.

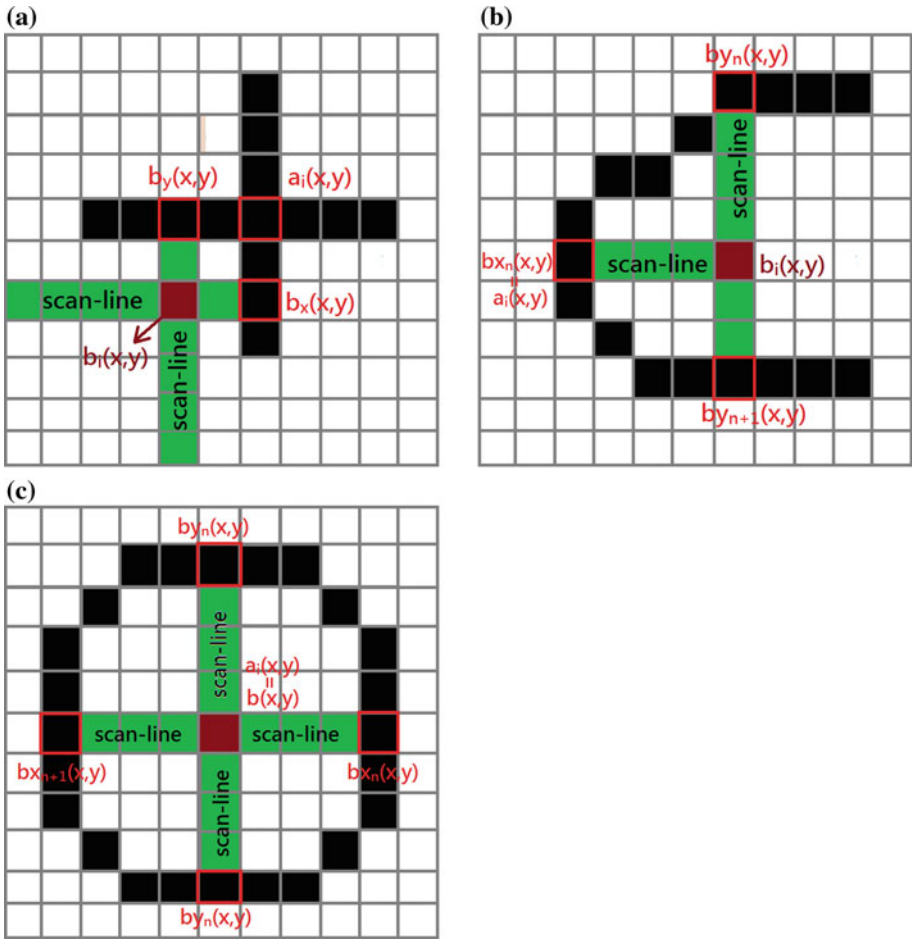

Fig. 3 Scenarios for identifying the OMGC **a** $p = 2$, and $n = m = 1$, **b** $p = 3$, and either $n = 1$, or $m = 1$, and **c** $p = 4$, $n = m = 2$

Figure 4 shows the detailed processing steps in searching for the initial boundary pixels by the IBPS. The objects' skeleton, the OMGC, and the end-points of the object's skeleton are shown in Fig. 4a. The IBPS then sets the OMGC as the origin of the scan-lines and t initial scan lines $L_i, i = 1.2.3 \ldots t$, where $t$is the number of the end-points of object's skeleton, are decided by emitting from the OMGC toward each end-point of the object's skeleton, as shown in Fig.4b.

In general, a boundary pixel, i.e., edge, of an object has a larger gradient value than the non-edges. Hence, in IBPS a 3×3 gradient-based operator, such as the Sobel operator, is masked on pixels along each scan-line from the end point to the boundary of a ROI in calculating the pixels' gradient, and the candidates for initial boundary pixels are determined by the criteria that the gradient of pixels on the scan line are larger than a pre-determined threshold and that the position of the initial boundary pixel is the nearest one to the end-point. The criteria of determining boundary pixels is describe as

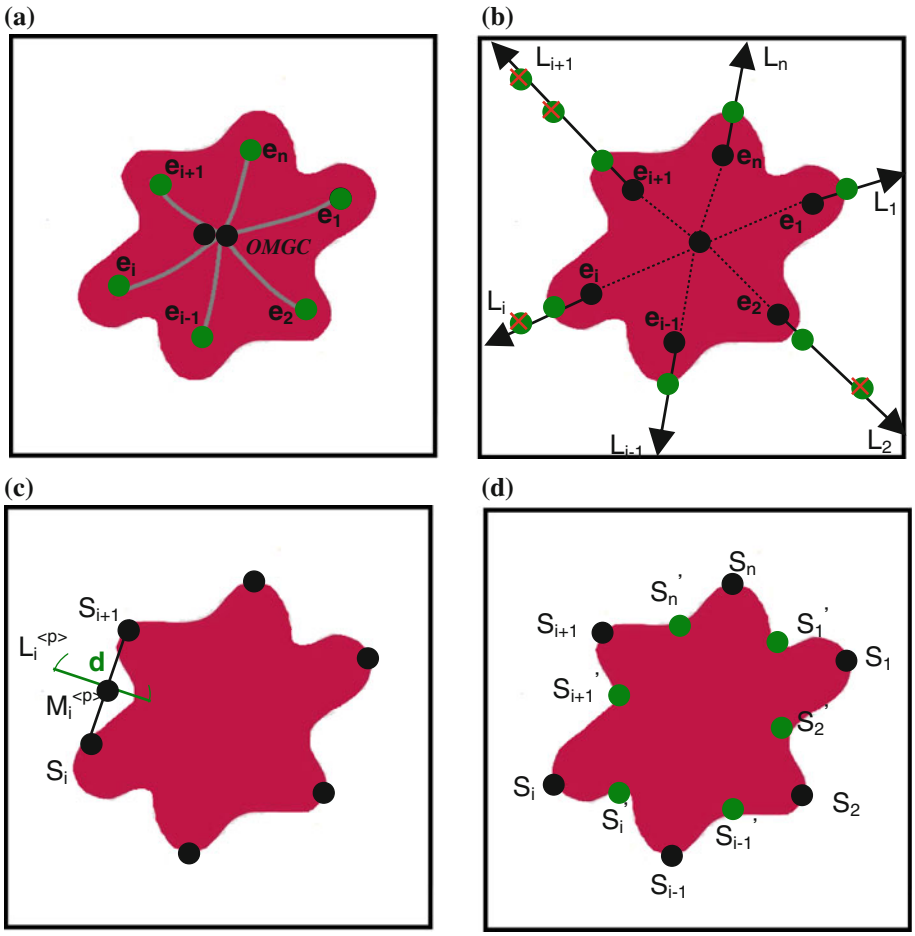

Fig. 4 Establishment of the scan-lines and initial boundary pixels selection: **a** an object with OMGC, skeleton and the end points of skeletone_i, **b** n initial scan-lines L_i are emitting from the OMGC through every end point of skelonton e_i, and the initial boundary pixel S_i is selected along each scan-lines, **c** mid-point between S_i and S_{i+1}, M_i, is determined to generate a new scan-line with new scan distance, d, for searching the new initial boundary pixels. **d** The complete set of initial boundary pixels S_n obtained by the IBPS

$$S_n = \begin{cases} CP_i, & \text{if (gradient value of scanned pixels} > \text{threshold)} \\ & \text{and (the distance to end point is minimum)} \\ Drop, & \text{otherwise} \end{cases} \tag{7}$$

where $CP_i, i = 1, \ldots, t$, is an array of initial boundary pixels. In (7), the threshold of the gradient value for each scan-line is selected by the gradient value of the pixel having the top 20% of pixels with highest ranked gradient values, i.e. gradient histogram, in each scanning segment. The solid dots on the convex tops along the scan-lines of Fig. 4b are the determined initial boundary pixels by (7). In order to obtain better resolution and more accuracy of the segmental contour following (SCF) results and to avoid noise effect in the ROI image, the number of initial boundary pixels can be increased iteratively by the following iterative initialization step to yield a complete set of initial boundary pixels, there having

$$N_{total} = t \times 2^p \tag{8}$$

of them where N_{total} is decided by t and p, the number of initial scan-lines and iteration times, respectively.

To increase the numbers of initial boundary pixels, the iterative initialization step in IBPS finds the middle point, denoted as $M_i^{<p>}$, between a pair of initial boundary pixels, S_i and S_{i+1}, selected in the previous initialization. The $M_i^{<p>}$ is then used as the base point to generate a new scan-line $L_i^{<p>}$, as shown in Fig. 4c. The position of $M_i^{<p>}$ is given by

$$\left(x_{M_i^{<p>}}, y_{M_i^{<p>}}\right) = \left\{(x, y)|x = \frac{\left(x_{s_{i+1}} + x_{s_i}\right)}{2}, y = \frac{\left(y_{s_{i+1}} + y_{s_i}\right)}{2}, i = 1, \ldots, t\right\} \tag{9}$$

where i is the index number of the scan-line and p is the iteration time. The new scan-line $L_i^{<p>}$ is in the direction of the normal vector to $\overrightarrow{S_i S_{i+1}}$ as shown in Fig.4c, and the linear equation normal to $\overrightarrow{S_i S_{i+1}}$ is calculated by the following

$$y - y_i^{<p>} = m_1\left(x - x_i^{<p>}\right) \tag{10}$$

where m_1 is the slope of new scan-line $L_i^{<p>}$, (x, y) represents positions on the scan-line $L_i^{<p>}$, and $\left(x_i^{<p>}, y_i^{<p>}\right)$ represents current position of middle point $M_i^{<p>}$. If, m_2 is the slope of $\overrightarrow{S_i S_{i+1}}$. $m_1$is perpendicular to m_2 and is given by $m_1 = -1/m_2$. According to the theory of linear equations, m_2 is formulated as $m_2 = \frac{y_{i+1} - y_i}{x_{i+1} - x_i}$. The more initial boundary pixels, iteratively selected by the iterative initialization step, are, the closer the new initial boundary pixels are to each other. Hence, the scan distance on the scan line can be decreased in each iteration and is given by

$$d = \frac{D}{2^{p-1}} \tag{11}$$

where D denotes default scanning distance and $d$will be decreased to half the distance of D in each iteration. After executing the IBPS process, the complete set of initial boundary pixels, S_n, are found as shown in Fig. 4d and the SCF is applied for the object contour extraction.

2.2 Segmental contour following (SCF)

To completely extract a closed object contour, the SCF is executed following the IBPS in the proposed ISCEM. The segmented contours, connected by any two neighboring initial boundary pixels, which were obtained by IBPS, will be extracted to form the complete closed contour of an object. The SCF employs the concept of gravitational force in combination with relative direction information between two neighboring initial boundary pixels in tracing along the object boundary. The flow chart of the SCF is shown in Fig. 5.

Figure 6 shows how the SCF proceeds by using the set of initial boundary pixels, obtained by IBPS, which separates the closed object contour into a segmented contour set, $\overline{S_{ij}}$ $i \in 1, \ldots, N-1$, $j = i+1$, as shown in Figure 6a, where each segmented contour between two neighboring initial boundary pixels is synchronously traced and linked through the SCF. Figure 6b demonstrates the relative direction from two neighboring initial boundary pixels,S_i to S_{i+1}, with S_i and S_{i+1} regarded as source and target boundary points, respectively. The relative direction, defined as the direction from source point S_i aiming at target point S_{i+1},

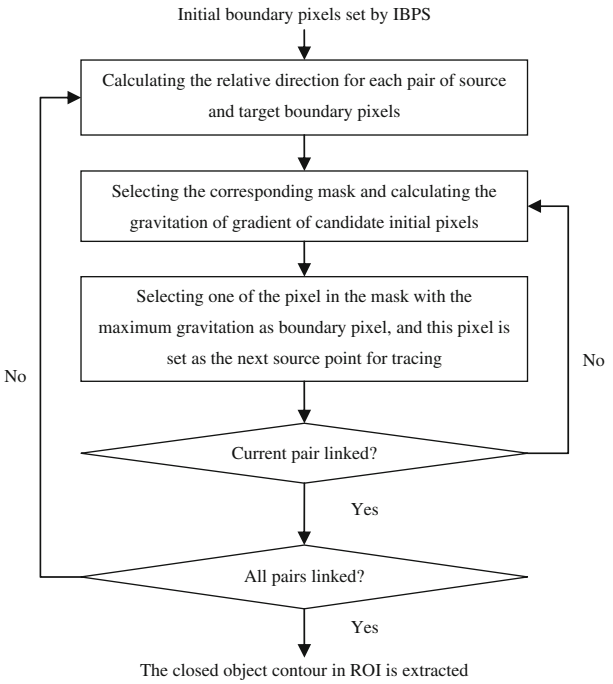

Fig. 5 Flowchart of the SCF mechanism

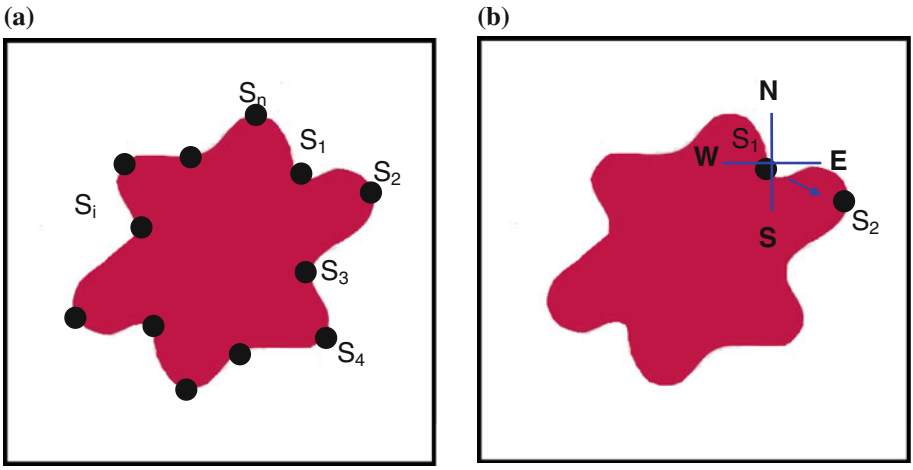

Fig. 6 The illustration of the SCF operation: **a** the initial boundary pixels obtained by the IBPS, **b** the relative direction among each pair of original and target contour pixels in tracing the possible contours in clockwise direction

can be derived by examining the sign of D_x and D_y, the distance between x_i and x_{i+1}, y_i and y_{i+1}, respectively, per calculation by

$$\begin{cases} D_x = x_{i+1} - x_i \\ D_y = y_{i+1} - y_i \end{cases} \tag{12}$$

Table 1 Nine states with the corrosponding relative direction

State	S	S–E	E	N–E	Null position	N	N–W	W	S–W
D_x	0	+	+	+	0	0	−	−	−
D_y	+	+	0	−	0	−	−	0	+

Note: + positive, *0* zero, − negative, *S* south, *N* north, *E* east, and *W* west, Null position means the origin and target points are the same one, i.e. segmented contour is found

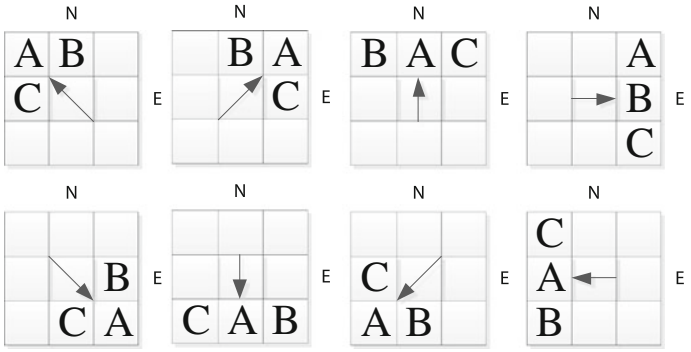

Fig. 7 Eight directional masks corresponding to the 8 relative directions

where (x_i, y_i) and (x_{i+1}, y_{i+1}) denote the positions of S_i and S_{i+1}, respectively. D_x and D_y are signed integer numbers and their sign is used to determine the relative direction from S_i to S_{i+1} as show in Table 1.

According to Table 1, the relative direction is classified with nine states and, except for the null position state, i.e., the target boundary pixel, each state is mapped to a directional mask, as shown in Fig.7.

In each directional mask, the center position of the mask is the source point, S_i, and A, B, C are the three candidate boundary pixels in the relevant directions, where one of the candidate pixels will be selected as boundary pixel and replaced as origin point for the next contour.

Under normal conditions without strong noise embedded in the image, the boundary pixel has a large intensity gradient which is caused by distinct intensity difference between the object and background. For selecting and tracing boundary pixels, the original pixel and target pixel are treated as two objects having gravitation force between them. According to Newton's law of gravitation, the heavier mass of an object and smaller distance between objects would have the larger magnitude of gravitation. Hence, in the SCF, the intensity gradient of pixels is regarded as the mass of an object. In selecting the next boundary pixel among the three candidate boundary pixels in the directional mask, the gravitation force between each candidate boundary pixels and the target pixel is calculated as the following

$$F_{(p)}(x_i, y_i) = \frac{\nabla f_p(x_i, y_i)}{\sqrt{\left(d_x^2 + d_y^2\right)}}, \; p \in A, B, C \tag{13}$$

where p is any one of the 3 candidate pixels in the directional mask, and $\nabla f_p(x_i, y_i)$ denotes the intensity gradient of pixel p at the position (x_i, y_i). In (13), the denominator represents distance between a candidate boundary pixel and a target boundary pixel (x_{i+1}, y_{i+1}). In each

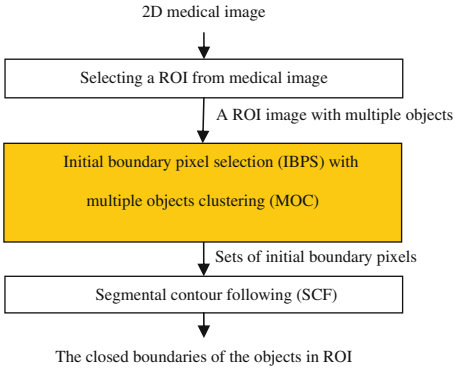

Fig. 8 The process flow diagram of the ISCEM extension for multiple object contour extraction within a ROI image

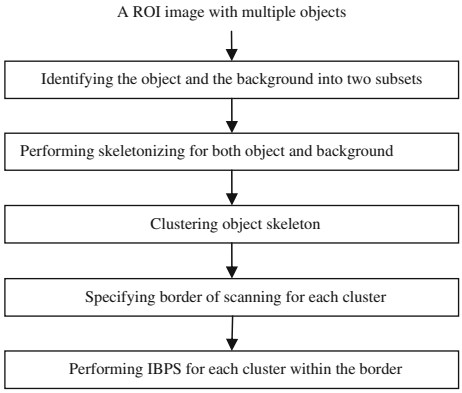

Fig. 9 The process flow diagram of the IBPS-MOC

iteration in tracing the boundary pixel within the segmented contour, the candidate boundary pixel with largest $F_{(p)}(x_i, y_i)$ value among three candidate boundary pixels is selected as boundary pixel and replaces the source point and the SCF proceeds until the target boundary point is reached within this segmented contour. Noting that the SCF is executed among any pair of neighboring initial boundary pixels selected by the IBPS such that each segmented contour can be traced and linked synchronously. This means is suitable for parallel processing in constructing a closed object contour within the ROI of medical images.

2.3 Extension of the ISCEM for multiple objects within a ROI image

By integrating a simple yet effective multiple objects clustering (MOC) algorithm with the IBPS, the ISCEM can be further extended for contour extraction of multiple objects within a ROI image. Figure 8 shows the process flow diagram of the extension of the ISCEM for multiple objects within a ROI image.

The IBPS with MOC, indicated in the inserted yellow rectangle of the process flow diagram in Fig. 8 and shown in Fig. 9 with detailed steps, is the key process for extending the ISCEM for multiple object contour extraction. The IBPS with MOC, named IBPS-MOC hereafter, first identifies the object and the background into two subsets and performs skeletonizing for both object and background. The IBPS-MOC then clusters the object skeleton pixels into sets of skeleton pixels with each object morphologically represented by each set of skeleton pixels, and the scanning border for each skeleton cluster is determined by the

background skeleton created in the previous step. The IBPS-MOC finally applies the IBPS to each cluster of skeleton with the pre-determined scanning border for the initial boundary pixels. Following the IBPS-MOC, the SCF traces the contour segments for each object to complete the contour extraction for multiple objects. The ISCEM extension for multiple objects is conducted on some real medical images and the results are presented in the next section.

The development of the ISCEM not only is particularly dedicated to the object contour extraction in medical images, but the consecutively incorporated edge-based initial boundary pixel searching along radiating scan-lines from the OMGC with the segmental contour following also is quite appropriate for gray-level medical images. In general, medical images are of gray scale with sparse gray levels, so an effective edge-based segmentation algorithm can be more suitable over the region-based segmentation ones. In addition, the inside of many human organs has clutters, their neighboring background textures appear relatively homogenous. Theoretically, skillful scanning for capably indicating representative object boundary edge nodes is the key issue for initial segmenting the object profile in a medical image. In this study, we incorporate two different scanning ways to increase the robustness of the IBPS. The first is scanning in radiation from the object's morphological geographic center. Due to neutralization by averaging effects and iterative searching, while finding the OMGC, the selection of a center can be robust against random noise, which is much more commonly met than burst noise in medical images. And our proposed IBPS is quite concise yet effective for the representation of objects in medical images with the radial scanning in multiple objects clustering (MOC). This technique can help in obtaining robustness of clustering skeleton pixels into groups in skeleton medical images.

3 Experimental results

3.1 Initial boundary pixel selecting results

To exam the accuracy of IBPS, artificial images with convex and a deep concave object are generated, as shown in Fig. 10. Because the positions of correct boundary are implicitly determined when the images are created, the accuracy of boundary point selection by the IBPS, can hence be evaluated by comparing with other existing methods. Figure 10a and c, respectively, show the original artificial convex and deep concave object images and Fig. 10b and d, respectively, show white Gaussian noise-added artificial convex and deep concave object images with SNR at 20.6 dB. The skeletons of the artificial convex and deep concave object images, obtained by the binarization and skeletonizing of the IBPS, are shown in Fig. 10b and d, respectively, as indicated by the white lines inside the images.

Experimental results of initial boundary pixel selection by the IBPS, the ISSM of our previous work, and method of Yuen et al. are shown in Fig.11. In IBPS, 6 and 4 initial scan-lines (end points) with 2 and 3 iterations are selected in determining 24 and 32 initial boundary pixels for the convex and deep concave object image, respectively. In ISSM 3, 4 initial scan-lines with 3 iterations are selected in determining 24 and 32 initial boundary pixels for the convex and deep concave object images, respectively. In the method of Yuen et al., 24 and 32 scan-lines are used to select the initial boundary pixels on the contours of the convex and deep concave object images, respectively. Figure 11a, and d demonstrate the initial boundary pixels selected by IBPS, where almost all the initial boundary pixels are exactly on the true edge and, even for the deep concave object image, only a few initial boundary pixels fall out of the true edges. Figure 11, middle column (Fig. 11b, e) and right

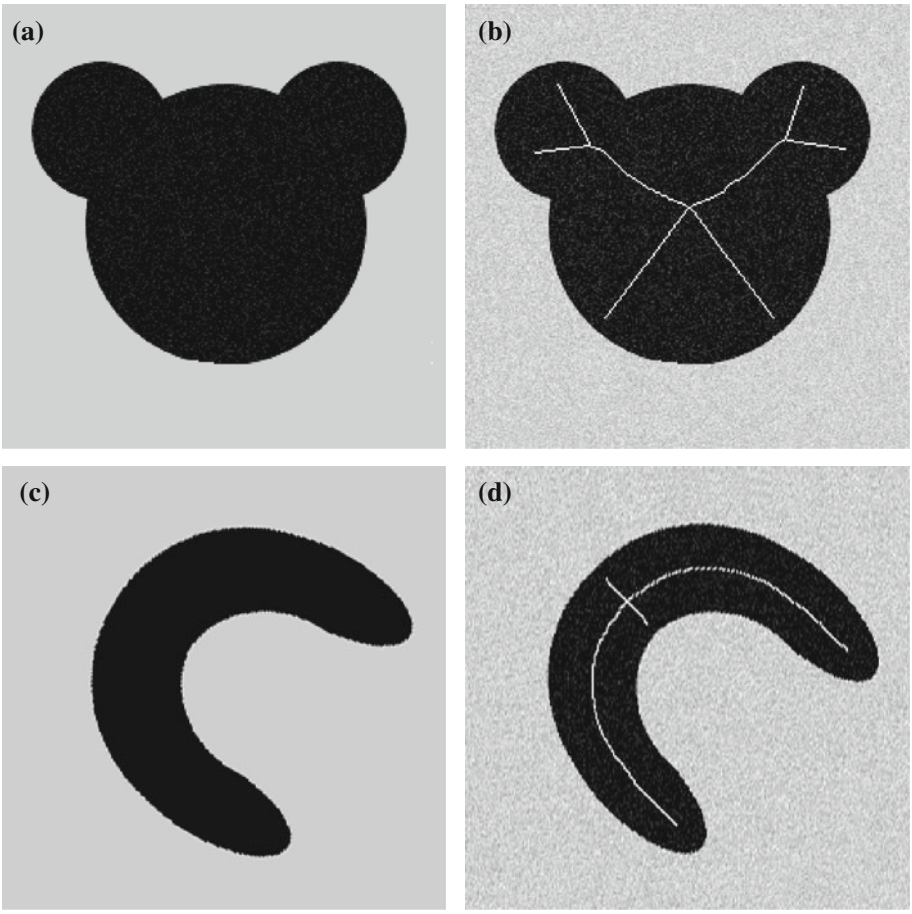

Fig. 10 Artificial images with noise-free (**a**) and the noisy (**b**) convex object, and with noise-free (**c**) and the noisy (**d**) deep concave object. The SNR in **b** and **d** is 25.3 dB

column (Fig. 11c, f), respectively, shows the initial boundary pixels selected, marked as a thick cross, by the ISSM and method of Yuen et al. for artificial images with convex and deep concave objects, where some initial boundary pixels are conceived to be erroneously selected and are far away from the boundary in artificial convex images. The numbers of erroneously selected initial boundary pixels increased most significantly especially for the deep concave object image.

To quantitatively compare the accuracy of IBPS, the ISSM, and the method of Yuen et al., the true positive is used as the comparing parameter and is defined as the ratio of true detected initial boundary pixels to total detected initial boundary pixels, whose results are shown in Table 2. According to Table 2, the IBPS obtained better accuracy in selecting initial boundary pixels among other initialization methods for both artificial images. It significantly outperforms other initialization methods especially for the artificial deep concave object image.

To further evaluate the relative locations of initial boundary pixels selected by IBPS, the ISSM, and Yuen's method, and their influence on the convergence of snake, mean distances, $\overline{d}$, and standard deviation, σ, between each neighboring initial boundary pixels are computed

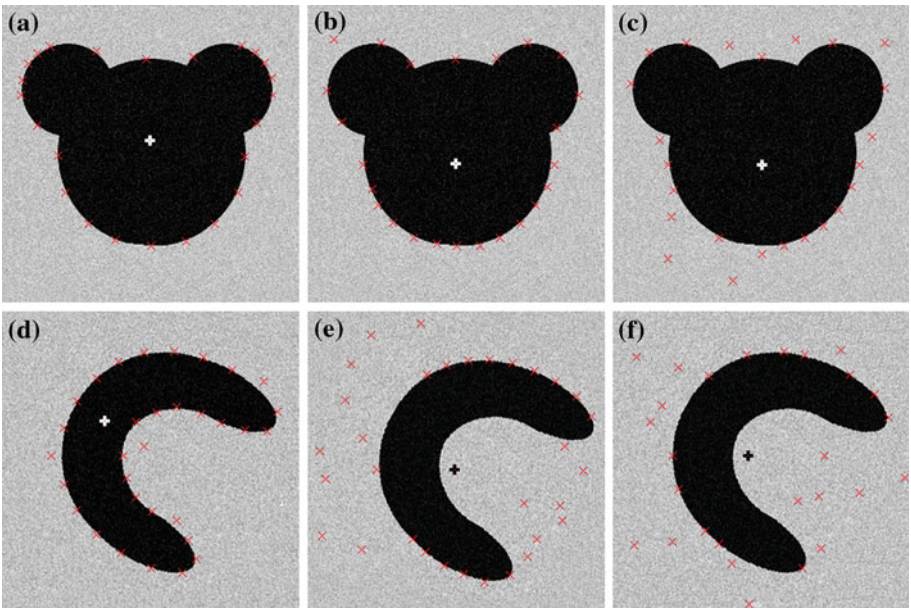

Fig. 11 Locations of initial boundary pixels for the two kinds of noisy artificial object images by different initialization methods with SNR = 25.3 dB: the *left column* **a** and **d** is the result of the proposed IBPS, the *middle one* **b** and **e** is the result of ISSM, and the *right column* **c** and **f** is the result of Yuen et al.

Table 2 Accuracy comparison of the IBPS, ISSM and Yuen et al. of the initial boundary pixel selection in terms of true positive

Image\method	IBPS	ISSM	Yuen et al.
Convex object	23/24	20/24	13/24
Deep concave object	27/32	16/32	11/32

Table 3 Statistical comparison of the initial boundary pixels selected by IBPS, ISSM and method of yuen et al. in terms of mean distance and standard deviation between each pair of selected neighboring boundary pixels

Method	IBPS		ISSM		Yuen et al.	
Image\parameters	$\overline{d}$	σ	$\overline{d}$	σ	$\overline{d}$	σ
Convex object	18.3	2.41	19.1	2.75	28.2	13.4
Deep concave object	23.4	2.94	34.6	13.9	40.3	17.9

as shown in Table 3 for both artificial images with convex and deep concave objects. The values of mean distance and standard deviation of each pair of neighboring boundary pixels selected by the IBPS are far smaller than these of the ISSM and the method of Yuen et al., which indicates that the initial boundary pixels selected by IBPS are closely and evenly located. By inspecting Fig. 11 and Table 3, one can find that the Yuen et al. method searches farthest edge pixels along each angle-fixed scan-line, hence it lacks flexibility and is easily affected by noise. The ISSM achieves better initial boundary pixels in comparison with that of Yuen et al. for the artificial concave image, however, the ISSM fails to precisely locate the initial boundary pixels for the deep convex image because the scan-lines are emitted from

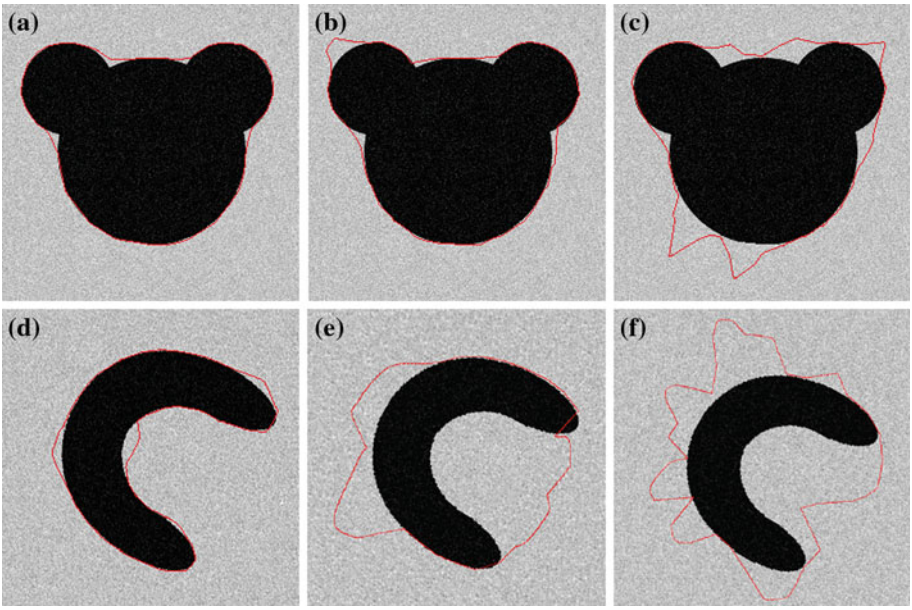

Fig. 12 The snake results for the artificial noisy convex and deep concave object images with SNR = 25.3 dB using the initialization results. The *left*, *middle* and *right columns* are the snake results using the initial boundary pixels selected by the IBPS, the ISSM, and the method of Yuen et al., respectively

the calculated CoG of the image which is out of the object's body. The IBPS on the contrary finds the initial boundary pixels by first searching the scan-lines emitting from the OMGC, which is inside the object's body, toward end points of a skeleton, and the searching distance of boundary pixel of each new scan-line is decreased in the iteration such that better accuracy in selecting initial boundary pixels can be achieved.

To demonstrate the influence of the set of initial boundary pixels, selected by IBPS, ISSM, and by the method of Yuen et al., in obtaining a closed object contour, the initialization results are further utilized for running snake. In executing snake, the locations of initial boundary pixels are gradually changed and controlled to close to the object contour, therefore the closer the selected initial boundary pixels are to the real object contour, the faster the snake converges and the higher the precision for the closed contour extracted with respect to the object's real contours. The extracted contour of snake utilized the initial boundary pixels, i.e., snaxels, selected by IBPS, ISSM, and the Yuen et al. method for the artificial convex and object images as shown in Fig.12. The left, middle, and right columns of Fig. 12 show, respectively, the snake results utilizing the initial snaxels obtained by the IBPS, the ISSM, and Yuen et al. Experimental results again demonstrate that the object contour extracted by snake for the artificial convex and deep concave object images utilizing the initial boundary pixels selected by IBPS is much closer to the real object's contour than those of both the ISSM and the Yuen et al. method because a lot of the initial boundary pixels selected by ISSM and Yuen et al. method are far from the true boundary such that an expanded closed object contour with extrusion is obtained when the snake converges.

To quantitatively compare the influence of the set of initial boundary pixels, selected by different initialization methods, in obtaining a closed object contour by the snake, the false positive is used as the comparing parameter and is defined as the ratio of the number of

Table 4 The false positive of the extracted contours by the snake using initial boundary pixels selected by different methods for the two artificial images

Images	Initialization methods (%)		
	IBPS	ISSM	Yuen et al.
Convex object	10.5	16.9	44.0
Deep concave object	11.9	70.5	76.5

Fig. 13 Real medical images for testing the proposed ISCEM. **a** A CT image showing two regions of interest, where the dimension in pixel of *ROI (1)* is 184 × 140 and *ROI (2)* is 126 × 133. **b** The MR image of brain core with one region of interest, *ROI (3)* with the dimensionality of 91 × 118

false detected initial boundary pixels to the number of total detected boundary pixels. The results of false positive of the three comparing methods for the convex and deep concave artificial images are shown in Table 4. According to Table 4, the IBPS has the smallest false positive among other initialization methods for extracting a contour by running the snake for both artificial images and significantly outperform other initialization methods especially for artificial deep concave object image.

To test the effectiveness of IBPS, the ISSM, and the method of Yuen et al. for real medical images, a CT image of pulmonary embolism and a T2 weighted MR image of the brain showing cortex, lateral ventricle, and falx cerebri, as shown in Fig. 13a and b, respectively, are used. This test CT medical image comes from a well-known medical database, MedPix, a free online medical image database, with image number 55,164, while the test MR image comes from Magnetic Resonance—Technology Information Portal. Three regions are selected as the regions of interest (ROI), two from the CT image and 1 from the MR image, and are numbered, within which the contour of the enhanced white objects in the ROIs are to be extracted.

Each of the ROI images with enhanced white object is processed by the IBPS, the ISSM, and the method of Yuen et al. for selecting the initial boundary pixels, i.e., snaxel initialization, and the results are shown in Fig. 14 with the marked red crosses representing locations of initial boundary pixel selected. Figure 14a–c, d–f, and g–i respectively, show the initial boundary pixels selected by the IBPS, the ISSM, and the method of Yuen et al. for ROI(1) and ROI(2) of the CT medical image, and ROI(3) of the MR medical image. By comparing with the ISSM, and Yuen et al. results of Fig. 14d–f, and g–i, respectively, it can be easily identified that the initial boundary pixels selected by IBPS, as in Fig. 14a–c, are much closer to the object's boundary in all three ROIs, while many of the snaxels selected by ISSM and the method of Yuen et al. are located in the darker background area. In examining the results

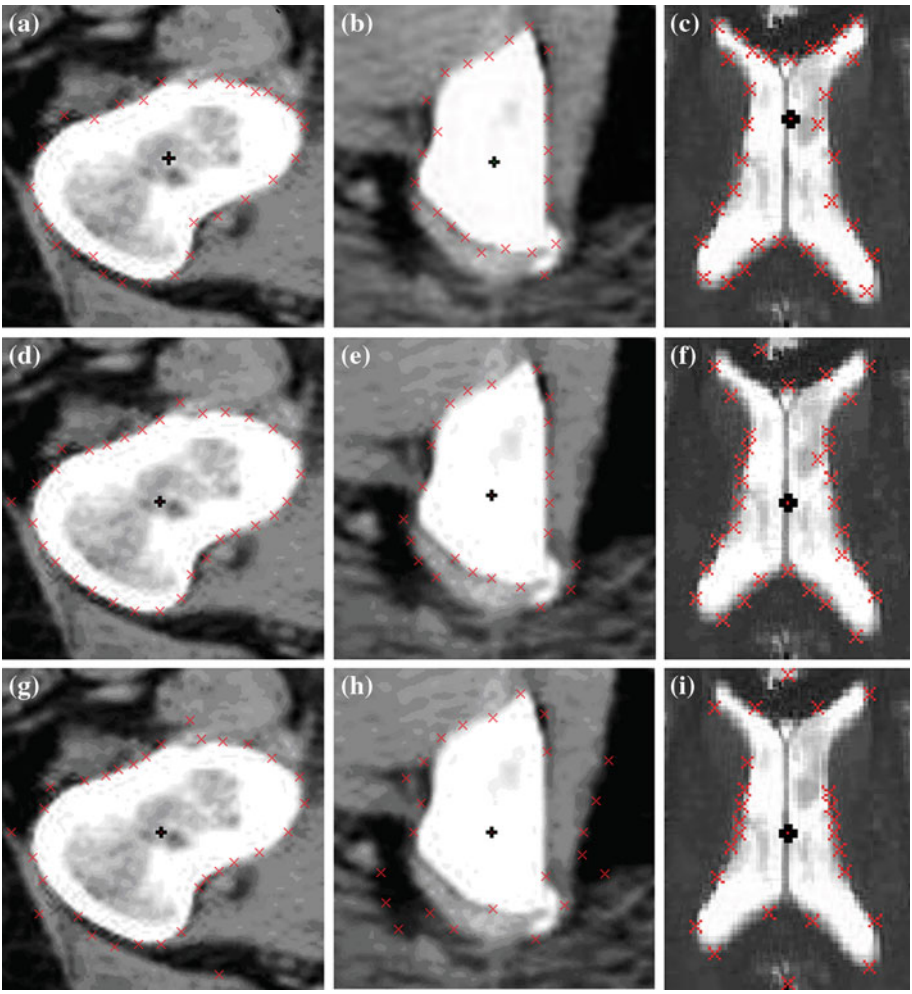

Fig. 14 The experimental results of the initial boundary point selection for the three ROIs from real CT and MR image of Fig 13. The *upper row* **a–c** shows the results of the IBPS for the three ROIs. The *middle row* **d–f** is the results of ISSM. The *bottom row* **g–i** is the results of Yuen et al.

of initial boundary pixels selected by the IBPS, the ISSM, and the method of Yuen et al., the results shown in Fig. 14b, and e appear critical because the lower left of the test ROI (2) image exhibiting a shading tissue occulted by a target object. By the proposed IBPS, the contour extraction of the target object in the lower left area can still be easily accomplished; however, the ISSM tends to extract the contour of the outer shading tissue. This is because the IBPS searches the boundary pixel along the scan line, connected by OMGC and the end point of object skeleton, from the end point toward the boundary and finds the nearest pixel, having greater gradient value than a pre-determined threshold, to the end point. On the contrary, the ISSM searches the boundary pixel along the scan line emitting from CoG and finds the farthest pixel, having greater gradient value than a pre-determined threshold, from the CoG.

The results of initial boundary pixels selected by the IBPS, the ISSM, and the method of Yuen et al. for the three ROIs from CT and MR medical images, as in Fig. 14, are again used

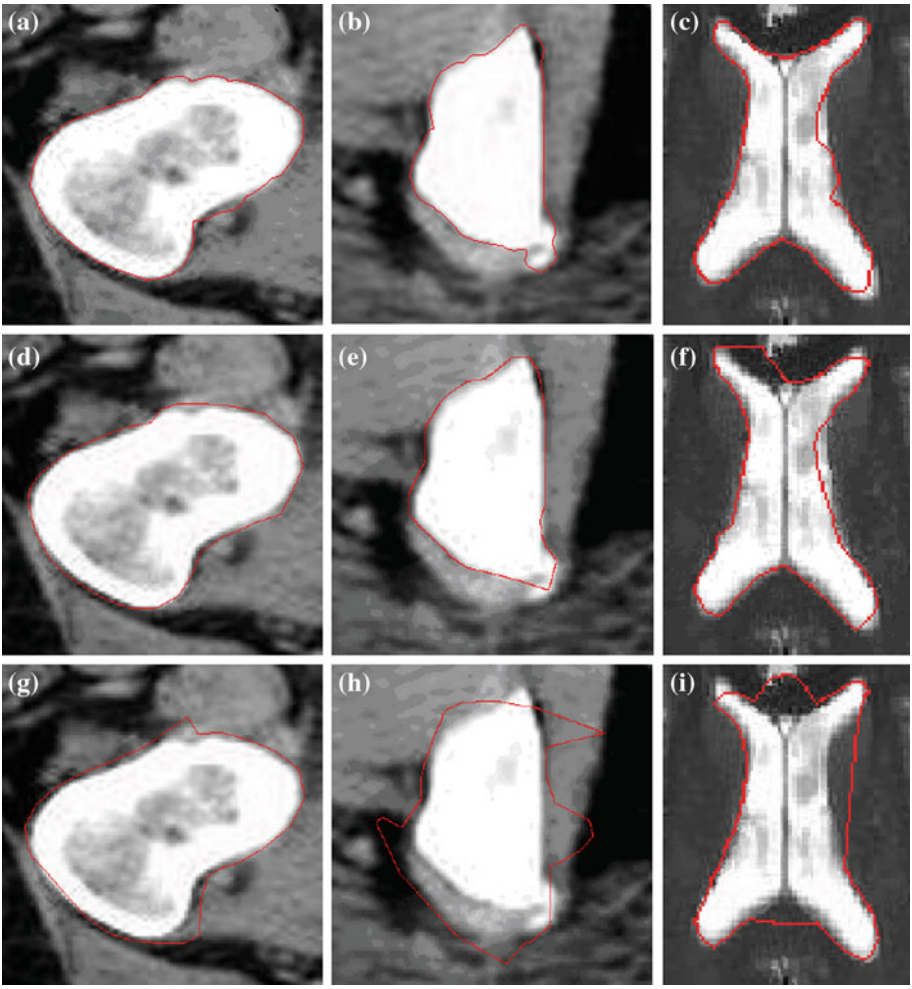

Fig. 15 The experimental results of running the snake using the initial boundary points in Fig. 14. The *upper row* (**a–c**), the *middle row* (**d–f**), and the *bottom row* (**g–i**), respectively, show the snake results using the initial boundary points selected by the IBPS, ISSM, and method of Yuen et al.

to run the snake in obtaining a closed object contour and the results are shown in Fig. 15 for visual comparison. Figure 15a–c, d–f, and g–i, respectively, show the snake result with initial boundary pixels selected by the IBPS, the ISSM, and the method of Yuen et al. By comparing Fig. 15a–c with Fig. 15d–f and g–i, it can be easily indicated that the snake results of the method of Yuen et al. are expanded with extrusion because many initial boundary pixels selected by the method of Yuen et al. are located far away from the distinct object boundary due to the noise and background influence. The snake results using snaxel initialization of the ISSM achieve a closer and smoother contour than those results obtained using the method of Yuen et al. On the other hand, the snake result using the IBPS selected initial boundary pixels, obtains a much more accurate contour than the other methods, which are noticeable by the extracted contour in upper part of object in Fig 15a, and c, and in the lower tail part of

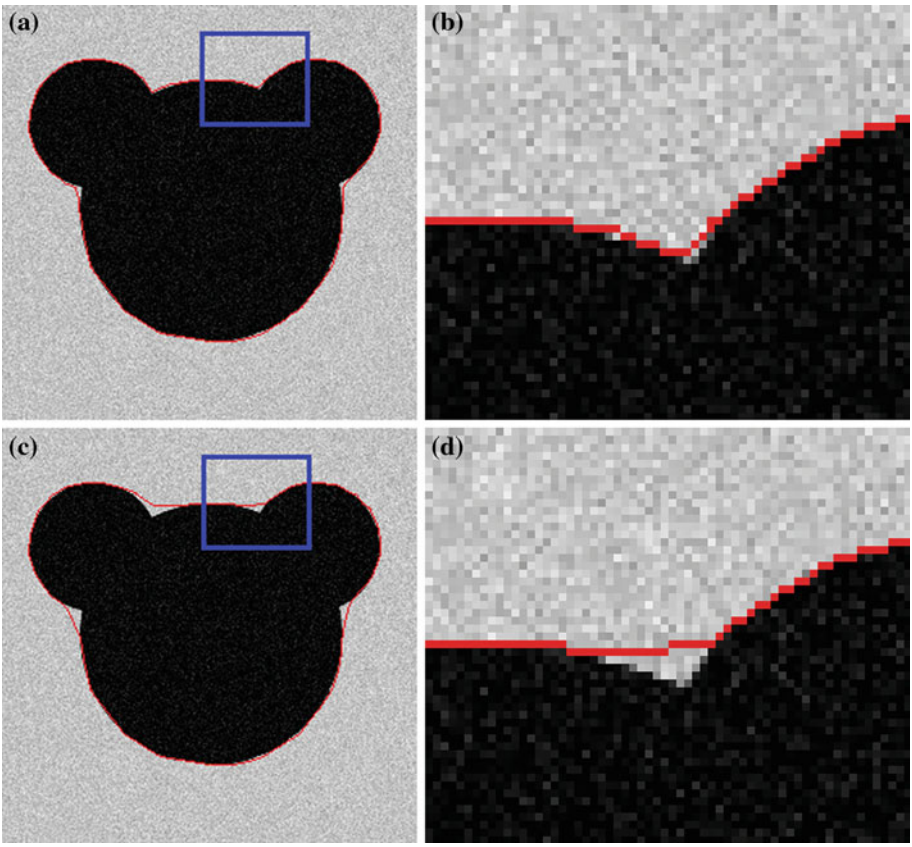

Fig. 16 Contour extraction result of SCF and Chen and Siy's boundary tracing method for artificial convex object image with SNR = 28.8 dB. **a** Contour extraction result of SCF and **b** the *magnified portion* around corner of (**a**). **c** Contour extraction result of Chen and Siy's boundary tracing method, and **d** the *magnified portion* around corner of (**c**)

Fig. 15b. It again demonstrates that the accurate initial boundary pixels selected by the IBPS leads to a better snake result for real medical image as well.

3.2 Segmental contour following results

To investigate the accuracy and effectiveness of SCF for contour extraction, experimental results of SCF and Chen and Siy's boundary tracing method (Chen and Siy 1987) for the artificial images of convex shape are first compared using the same set of initial boundary pixels selected by the IBPS. Figure 16 shows the results of contour extraction, as pixels shown in red, for the artificial images of convex shape with white Gaussian noise added. The SNR is 28.8 dB. The left-hand side of Fig.16a and c, respectively, demonstrates the contour extracted for the artificial convex shape image for SCF and Chen and Siy's method, while the right-hand side of Fig. 16 is the magnified corner portion of tracing results inside the rectangle in the left figure. Experimental results of Fig. 16a and c exhibit that the SCF traces on the real object boundary in constructing a closed object contour matching to the object's

Table 5 Quantitative comparison in terms of true positive for the artificial convex shape image with different levels of white Gaussian noise added

Methods SNR\precision (dB)	SCF (%)	Chen and Siy's method (%)
28.8	98	84
25.2	97	83
20.6	95	83

true contour, while there are some detected pixels by Chen and Siy's method which deviate from the true boundary.

Table 5 shows the quantitative comparison in terms of true positive by testing SCF and Chen and Siy's boundary tracing method utilizing the initial boundary pixels selected by the IBPS for the artificial convex shape image with different levels of white Gaussian noise added. The true positive is defined as the ratio of the number of true detected boundary pixels to the total number of detected boundary pixels. By examining Table 5, the true positives of contour extraction result by SCF is about 12∼14% better than those of Chen and Siy's tracing method for the artificial convex shape image with different levels of white Gaussian noise added. It again demonstrates the advantage of SCF in integrating the intensity gradient and relative direction for contour tracing, which provides more local structure information when compared to Chen and Siy's tracing method, which relies on magnitude of gradient only in determining contour direction.

To further examine the effectiveness and efficiency of the ISCEM for contour extraction in a real medical image of Fig. 13, the extraction results of SCF are comparing with Chen and Siy's tracing method using the same set of initial boundary pixels selected by IBPS for the 3 ROIs images from the medical images. To compare with the contour extraction results of the ISCEM, the contour extraction method of ISSM + SCF from our recent work is conducted as well for the three ROI images. Contour extraction results of three ROI images for the three comparing methods are shown in Fig.17. Figure 17a–c, and d–f, respectively, show the results of the proposed SCF, and the Chen and Siy's boundary tracing method utilizing the same set of initial boundary pixels selected by IBPS. The contour extraction results of ISSM + SCF of our previous work for the three ROI images are presented in Fig. 17g–i. By examining on the contour extraction results of Fig. 17, one can see that the closed object contour of each ROI image is extracted by SCF utilizing the initial boundary pixels found by the IBPS However, unlike the closed contour extraction result of the artificial convex images, Chen and Siy's tracing method fails to obtain the closed object contour for the three real medical ROI images. The contour extraction results of the proposed ISCEM (i.e., IBPS+SCF) in Fig. 17a–c and those of ISSM+SCF resulting in Fig. 17g–i have the comparable extraction results; however, the ISCEM traces more details of the object's contour with much higher precision than from ISSM+SCF, as shown in the right waist part in Fig. 17a, lower right tail part in Fig. 17b, and upper concave part in Fig. 17c. Table 6 shows the execution time for three comparing methods of the proposed ISCEM, the ISSM+SCF, and the IBPS+Chen and Siy's method, where the proposed ISCEM has comparable computational time with that of IBPS+Chen and Siy's method. The ISCEM only takes about one third of the ISSM+SCF computational time, which is significantly decreased due to the efficiency of binarization and skeletonizing, and OMGC computing. By examining the contour extraction results of Fig. 17 and Table 6 for the three comparing method, one sees that the ISCEM has the advantage of extracting a closed object contour with high definition and precision at a significant time decrease for real medical images in comparing with the ISSM+SCF of our earlier work. And even though

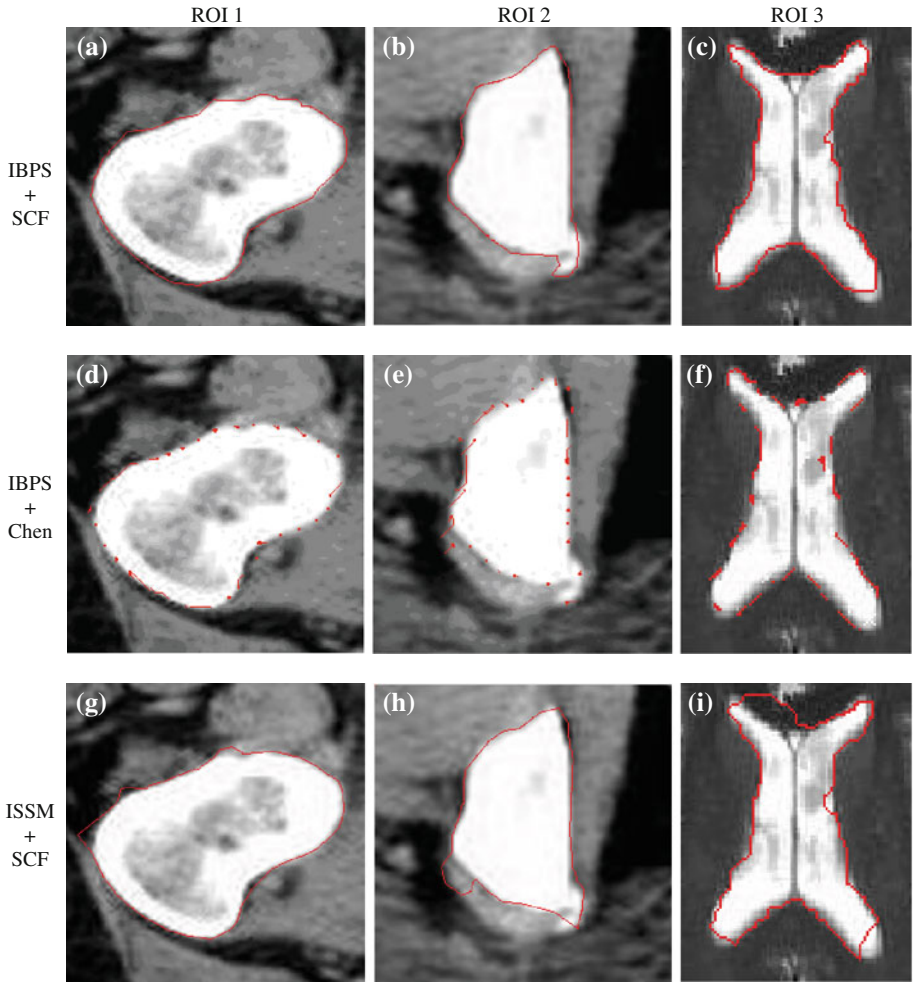

Fig. 17 Contour extraction results of **a–c** SCF, and **d–f** Chen and Siy's boundary tracing method using the same set of initial boundary pixels selected by IBPS for each ROI in medical images of Fig. 13. **g–i** Contour extraction results of SCF using initial boundary pixels selected by ISSM for each ROI in medical images of Fig. 13

a closed contour for artificial object is obtained by Chen and Siy's boundary tracing method, yet it fails to produce a closed contour for real medical images possibly due to the noise, and the local structure complexity between the object and background with larger computational time than the proposed ISCEM.

3.3 Results of ISCEM extension for multiple objects within a ROI image

Experiment of the ISCEM extension for multiple objects within a ROI image is performed for multiple objects in CT images as shown in Fig. 18 and the related results on the output of each step in Fig. 9 for the ROI medical image of Fig. 18a are shown in Fig. 19.

Table 6 Execution time measurement of boundary extraction from three comparing methods for three ROIs in medical image, the unit of the execution time is in millisecond (ms)

ROI	Methods (ms)		
	IBPS+SCF	IBPS+Chen and Siy	ISSM+SCF
1	90	102	255
2	74	97	233
3	65	78	168

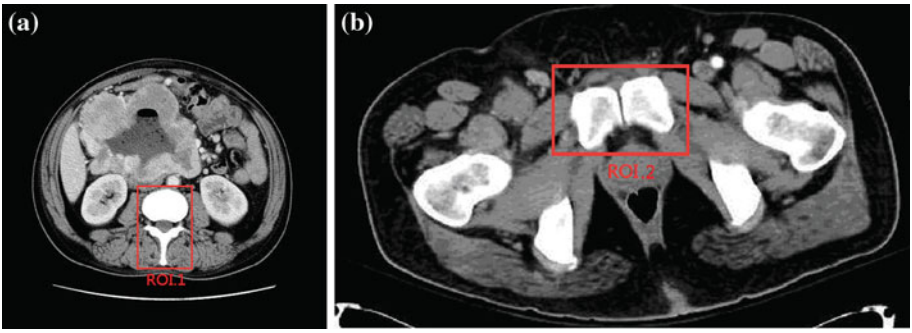

Fig. 18 The tested CT imageries for the ISCEM extension for multiple objects. **a** The selected *ROI 1* showing the vertebra body and vertebra spinous process from the CT image, **b** the selected *ROI 2* with two enhanced objects from the CT image of pulmonary embolism

Figure 18a and b, respectively, show the selected ROI 1 (region of vertebra body and vertebra spinous process) from a CT image and the selected ROI 2 with two enhanced objects from the CT image of pulmonary embolism in Fig. 13. Figure 19 shows the experimental results of each step in Fig. 9 for the ROI 1 image with two objects. Figure 19a and b, respectively, show the original ROI image with two objects and the result of step 1, identifying the object and background into two subjects. Figure 19c and d, respectively, show the result of performing skeletonizing on the object and on the background, as is specified in step 2. The scanning border of each cluster, as the step 4 of the Fig. 9, is hence obtained by the skeleton of the background and is shown in Fig. 19d. Figure 19e and f, respectively, show the cluster of object skeleton, the 3rd step in Fig. 9, and the result of the IBPS-MOC, the last step in Fig. 9. Figure 20 shows the experimental results of the proposed ISCTM extended to multiple objects for the two ROIs in Fig. 18. The left column (Fig. 20a and d) is the result of clustering a skeleton with a distinct border in separating each skeleton cluster. The middle column (Fig. 20b and e) shows the sets of initial boundary pixels, indicated with red and blue "x" sign, selected by IBPS and with OMGCs indicated with dark "+"sign. The right column (Fig. 20c and f) is the result of SCF utilizing the initial boundary pixels selected by the IBPS-MOC, i.e., the contour extraction results of ISCEM extended to multiple objects for real medical images, whose contour is indicated by red and blue color for different objects. In examining the results of multiple object contour extraction, the case shown in Fig. 20d appears critical because the test ROI image exhibiting two extreme contiguous tissues of an organ with background clutters. By the proposed scheme, the contour extraction of the two contiguous tissues can still be easily accomplished without *a-priori* human-supporting knowledge. In short, increased computational complexity of the IBPS-MOC merely is rare or unnoticeable,

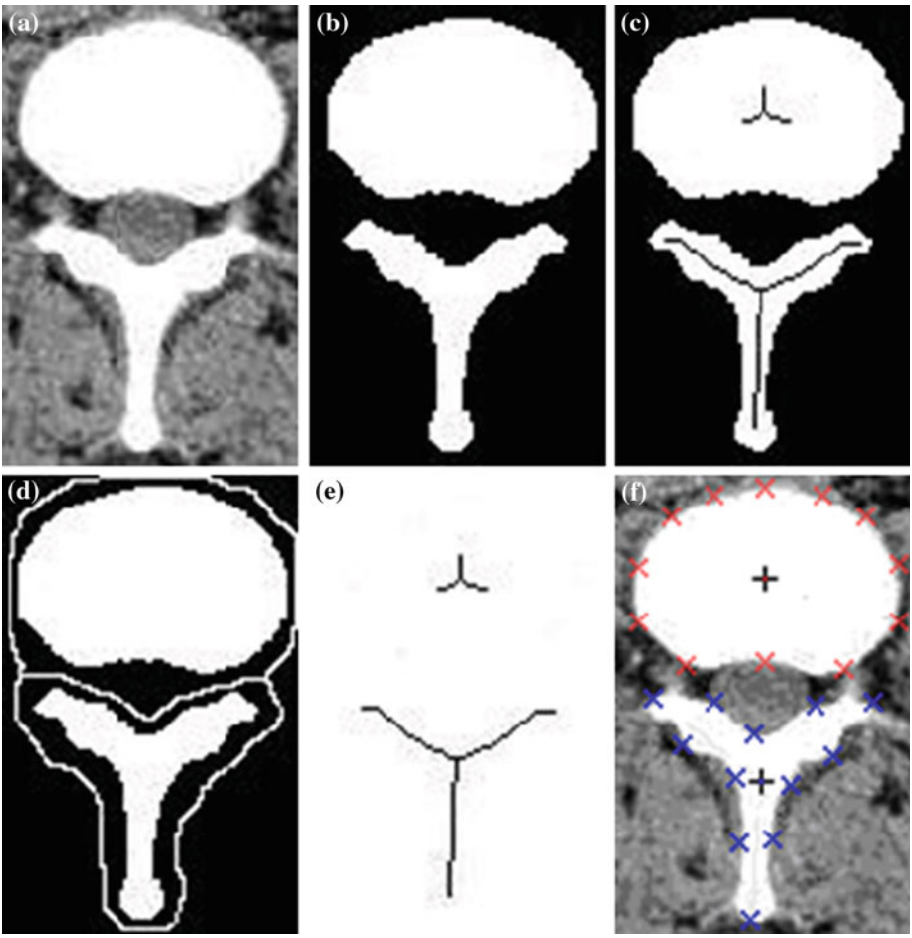

Fig. 19 The experimental results of each step of the proposed IBPS-MOC, as in Fig. 9, for an example ROI image with two objects. **a** and **b**, respectively, show the original ROI image with two objects and the result of step 1, identifying the object and background into two subjects. **c** and **d**, respectively, show the result of performing skeletonizing on the object and on the background, as specifying in the step 2. The scanning border of each cluster, as the step 4 of the Fig. 9, is hence obtained by the skeleton of the background and is shown in **d**. **e** and **f**, respectively, show the clusters of object skeleton, as the 3rd step in Fig. 9, and the result of the IBPS-MOC, as the last step of Fig. 9

even when the content of the medical image exhibits noticeable complication. This is because the mechanism of proposed IBPS-MOC is quite regular and concise. By examining Figs. 8, 9 and 20, one can see with only a few modifications to the IBPS with multiple objects clustering, that the extension of ISCEM can efficiently and effectively extract contours for multiple objects within a ROI image with much higher precision.

To prove the feasibility and novelty of the proposed ISCEM and ISCEM-MOC, more ROI images are selected from the original medical images, as shown in Fig. 21, and tested using the ISCEM and ISCEM-MOC, and the experimental results are shown in Fig. 22.

Figure 22a, b, and c, respectively, shows the results of object skeleton, the IBPS results, and the ISCEM/ISCEM-MOC results of the ROI images, where the results of the ROI images

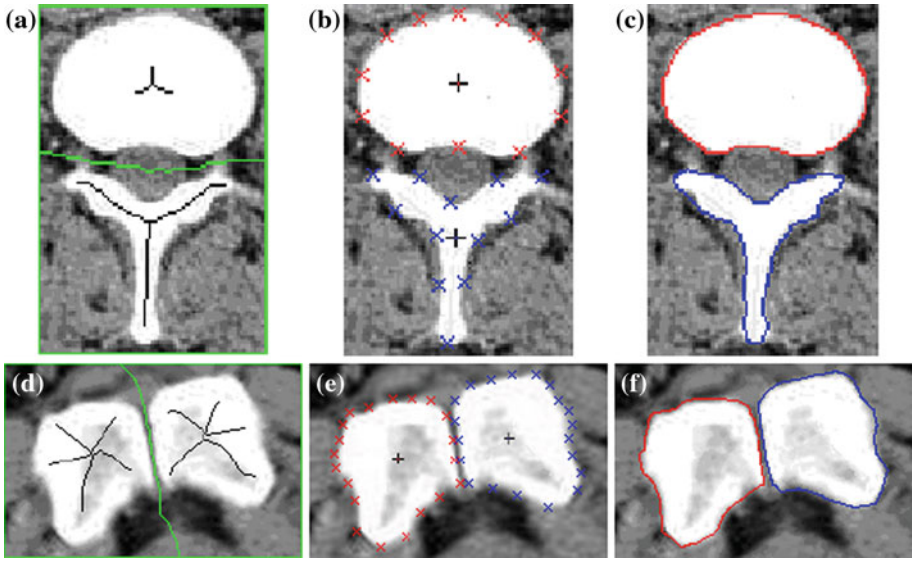

Fig. 20 The experimental results of the proposed ISCTM with extension to multiple objects within a ROI image. The *left column* **a** and **d** is the result of clustering a skeleton with a distinct border in separating each skeleton cluster, the *middle column* **b** and **e** shows the sets of initial boundary pixels selected by IBPS with OMGCs, and the *right column* **c** and **f** is the result of SCF utilizing the initial boundary pixels selected by the IBPS-MOC

with two objects, selected from the right medical image of the first column in Fig. 21, are shown in the ROI images of the third and the fourth column of the second row in Fig. 22a–c. By examining the object skeleton and IBPS results of Fig. 22a and b, respectively, one sees that the IBPS/IBPS-MOC can easily and automatically obtain object skeleton(s) with at least 6 end points and the initial boundary pixels even for object(s) with long strip shape such as the four ROI images in the second row of Fig. 22a. The experimental results of Fig. 22c shows that accurate object contours are delineated by the proposed ISCEM/ISCEM-MOC, where the contour extraction of the two contiguous tissues of an organ, in the ROI images of the third and the fourth column of the second row in Fig 22c, can still be easily accomplished without a-priori human-supporting knowledge. The experimental results on these ROI medical images again provide the evidence that the proposed ISCEM/ISCEM-MOC not only is novel to the area of multiple objects contour extraction in medical images, but it is also effective, efficient, and accurate in extracting object(s) contour in medical images.

In summary, the globally optimized contour extraction algorithms such as the graph cut/grabcut and snake discussed in Sect. 1 may truly yield better precision at the cost of time for the object contour extraction in medical images. However, the proposed ISCEM/ISCEM-MOC could achieve the similar precision for the same ROI images with the reduced computational complexity and computing time due to the inherent conciseness and robustness of the consecutive yet tightly integrated IBPS and SCF structure. Basically, the designing of an efficient algorithm can be considered as solving a constrained optimization problem. The processing cost including the structure complexity of the algorithm and the computational time, and so forth is minimized subject to an acceptable accuracy or adequate precision (a rational limitation or requirement). For object contour extraction in grey-level medical images, the ISCEM/ISCEM-MOC, a regular structure and concise processing flow of

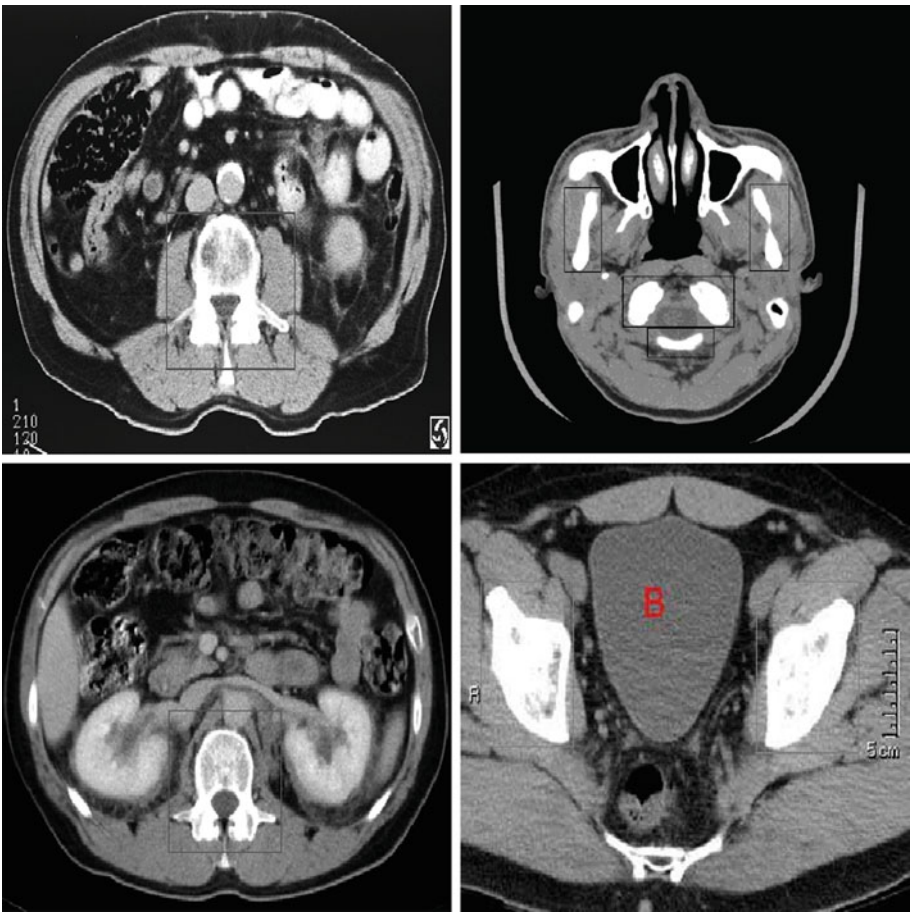

Fig. 21 Medical images with selected ROI, as indicated by the *rectangular boxes*, for testing the proposed ISCEM and ISCEM extended to multiple objects, where two selected ROI images with two objects are selected from the right medical image of the *first column*

proposed algorithm subject to such a limitation (requirement), could be granted to reach a solution of a constrained optimization algorithm by observing the experimental results. So, strictly speaking, the graph cut/grabcut model and the snake ones are considered as quite different approaches from the proposed one from the aspect of accomplishing specified goal (issue) and source-dependent applicability (fitness). Besides, execution of a concise and efficient algorithm for medical images on a medical computer/server tends to conserve more energy (i.e., attain higher power-saving effect), produce less hazardous gas emitting from a working motherboard and maintain the nominal environmental temperature, which comply with the current issue and trend of green computing and green IT. Moreover, considering execution of the concise, energy-efficient yet effective ISCEM/ISCEM-MOC for gray-level medical images over a large scale of computers/servers equipped at clinics, hospitals, medical schools, and physical examination centers, not only the objective of accurate contour extraction for gray-level medical images are attained but the purpose of environmentally sustainable computing also would be served.

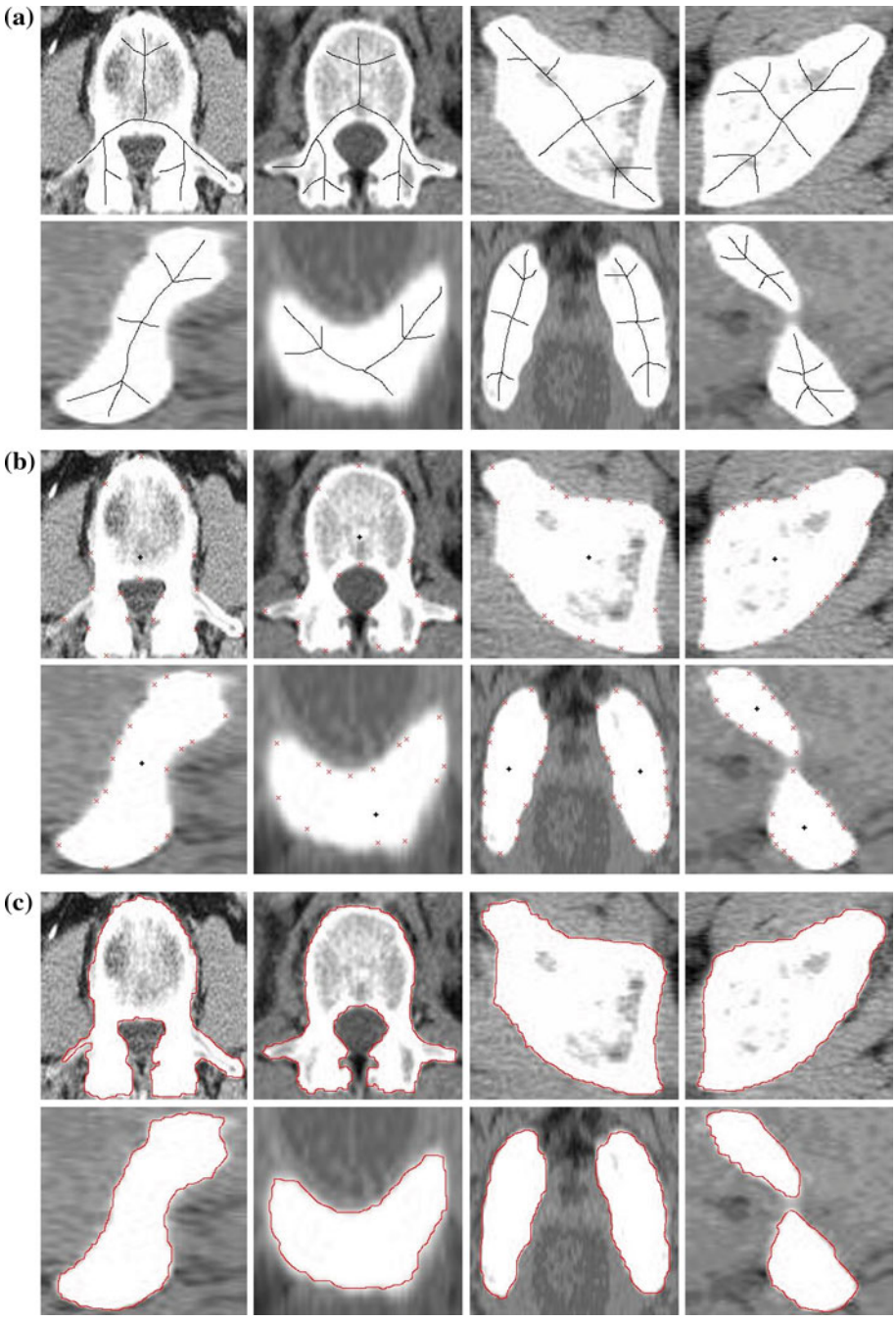

Fig. 22 The experimental results of the proposed ISCEM and ISCEM extended to multiple objects. **a**, **b**, and **c**, respectively shows the results of object skeletons, the IBPS and the ISCEM, where the results of the ROI images with two objects, selected from the *upper right* medical image in Fig. 21, are shown in the *lower right* of **a**, **b**, and **c**

4 Conclusions

In this paper, an initial boundary pixel selection (IBPS) and segmental contour following (SCF), proposed for object contour extraction within ROI in gray-level medical images, is presented. The IBPS automatically searches efficiently for initial boundary pixels along initial scan lines and then iteratively generates new scan lines in between the previous pairs of initial boundary pixels for searching for initial boundary pixels. Following the IBPS, the SCF effectively traces each segmented contour formed by a pair of neighboring initial boundary pixels found by the IBPS, by employing the concept of gravitational force and relative direction, in constructing a closed object contour. The major contributions of the proposed object extraction method are the automatic initialization of initial boundary points and the efficiency in synchronously searching and following each segmented contour in constructing a closed contour with high precision. Moreover, with a few modifications in the IBPS, the ISCEM is extended for contour extraction of multiple objects without changing the overall structure. Besides, the IBPS has the characteristics of being independent of boundary detection methods, hence, IBPS can also be applied to handle the contour initialization problem in an active contour model or for other contour following methods. Consequentially, since the proposed ISCEM possesses a highly regular structure for object(s) contour extraction of medical images, its complexity is only slight raises with an increase of the processed medical image complexity.

References

Bakir, H., & Charfi, M. (2009). Automatic medical image segmentation based on EPGV-SNAKE. In *Proceedings SSD '09: IEEE International Multi-Conf. System, Signals and Devices,* (pp. 1–5). 23–26 March 2009.

Banerjee, C., Pandey, G., & Namdeo, H. K. (2010). Contour following using maximum search algorithm, In *Proceedings ICSAP '10:IEEE International Conf. Signal Acquisition and Processing*, (pp. 295–297). 9–10 Feb 2010.

Boykov, Y., & Jolly, M.-P. (2011). Interactive graph cuts for optimal boundary and region segmentation of objects in n-d images. In *Proceedings ICCV'01: International Conference on Computer Vision*, (pp. 105–112). Canada, July 2001.

Canny, J. F. (1986). A computational approach to edge detection. *IEEE Transactions on Pattern Analysis and Machine Intelligence, 6*(6), 679–698.

Chan, D.-Y., & Hsu, R. C. (2008). Robust shape-preserving contour tracing with synchronous redundancy pruning. *Pattern Recognition Letters, 29*, 569–579.

Chan, D.-Y., Hsu, R. C., Jhuo, J.-C., Kao, B.-W., & Liu, C.-T. (2009). Polygon approximation for snake initialization in noisy image. In *Proceedings WCVIM '09: International Workshop on Computer Vision and Its Application to Image Media Processing*. 13 January 2009.

Chen, B. D., & Siy, P. (1987). Forward/backward contour tracing with feedback. *IEEE Transactions on Pattern Analysis and Machine Intelligence, 9*(3), 438–446.

Chuang, C. H., & Lie, W. N. (2001). Automatic snake contours for the segmentation of multiple objects. In *Proceedings ISCAS '01: IEEE International Symposium on Circuits and System*, (Vol. 2, pp. 389–392). 6–9 May 2001.

Dang, H., Hong, Y., Fang, X., & Qiang, F. (2009). Initial contour automatic selection of geometric active contour model. In *Proceedings ICICTA '09: IEEE International Conf. Intelligent Computation Technology and Automation*, (Vol. 2, pp. 66–69). 10–11 Oct 2009.

Delmas, P., Coulon, P.Y., & Fristot, V. (1999). Automatic snake for robust lip boundaries extraction. In *Proceedings ICASSP '99: IEEE International Conf. Acoustics, Speech, and Signal Processing* (Vol. 6, pp. 3069–3072). 15–19 March 1999.

Fu, K. S., & Mui, J. K. (1981). A survey on image segmentation. *Pattern Recognition, 13*(1), 3–16.

Gonzalez, R., & Woods, R. (2008). *Digital image processing* (3rd ed.). Englewood Cliffs, NJ: Prentice Hall.

Guo, Z., & Hall, R. W. (1989). Parallel thinning with two-subiteration algorithms. *ACM, 32*, 359–373.

Handels, H., Meinzer, P. H., Deserno, T. M., & Tolxdorff, T. (2010). Advances and recent developments in medical image computing. *International Journal of Computer Assisted Radiology and Surgery, 5*(6), 555–556.

Hsu, R. C., Chan, D.-Y., Kao, B.-W., & Liu, C.-T. (2010a) An automatic snaxel initial selection method in active contour model for contour extraction, 2010. In *International Conference on Image Processing (ICIP)*, (pp. 3017–3020). Sept 26–29, 2010.

Hsu, R. C., Kao, P.-W., Lai, W.-J., & Liu, C.-T. (2010b) An initial edge point selection and segmental contour following for object contour extraction. In *The 11th International Conference on Control, Automation, Robotics and Vision, ICARCV 2010,* (pp. 1632–1637). 7–10 Dec 2010.

Kass, M., Witkin, A., & Terzopoulos, D. (1988). Snakes: Active contour models. *International Journal of Computer Vision, 1*(4), 321–331.

Lehmann, T. M., Meinzer, H. P., & Tolxdorff, T. (2004). Advances in biomedical image analysis past, present and future challenges. *Methods of Information in Medicine, 43*(4), 308–314.

Lempitsky, V., Kohli, P., Rother, C., & Sharp, T. (2009) Image segmentation with a bounding box prior. In *Proceedings ICCV'09: International Conference on Computer Vision*, (pp. 105–112). Canada, July 2001.

Otsu, N. (1979). A threshold selection method from gray-level histograms. *IEEE Transactions on System, Man and Cybernetics, 9*, 62–66.

Pang, B., Zhang, D., & Wang, K. (2005). The bi-elliptical deformable contour and its application to automated tongue segmentation in Chinese medicine. *IEEE Transactions on Medical Imaging, 24*(8), 946–956.

Rother, C., Kolmogorov, V., & Blake, A. (2004). "GrabCut": Interactive foreground extraction using iterated graph cuts. *ACM Transaction on Graphs, 23*(3), 309–314.

Sakalli, M., Lam, K. M., & Yan, H. (2006). A faster converging snake algorithm to locate object boundaries. *IEEE Transactions Image Processing, 15*(5), 1182–1191.

Somkantha, K., Theera-Umpon, N., & Auephanwiriyakul, S. (2010). Boundary detection in medical images using edge following algorithm based on intensity gradient and texture gradient features. *IEEE Transactions on Biomedical Engineering*, TBME-00572-2010.R2.

Suzuki, K., Horiba, I., Sugie, N., & Nanki, M. (2004). Extraction of left ventricular contours from left ventriculograms by means of a neural edge detector. *IEEE Transactions on Medical Imaging, 23*(3), 330–339.

Teixeira, G. M., Pommeranzembaum, I. R., de Oliveria, B.L., Lobosco, M., & Santos, R.W. (2008). Automatic segmentation of cardiac MRI using snakes and genetic algorithms. In *Proceedings ICCS '08: International Conference on Computational Science*, Part III, LNCS 5103, (pp. 168–177). 23–25 June 2008.

Whithey, D. J., Pedrycz, W., & Koles, Z. J. (2009). Dynamic edge tracing: Boundary identification in medical images. *Computer Vision and Image Understanding, 113*(10), 1039–1052.

Xu, C., & Prince, J. L. (1998). Snake, shapes, and gradient vector flow. *IEEE Transactions Image Processing, 7*(3), 359–369.

Yan, P., & Kassim, A. (2006). Medical image segmentation using minimal path deformable models with implicit shape priors. *IEEE Transactions on Information Technology in Biomedicine, 10*(4), 677–684.

Yuen, P. C., Feng, G. C., & Zhou, J. P. (1999). A contour detection method: Initialization and contour model. *Pattern Recognition Letters, 20*(2), 141–148.

Author Biographies

Roy Chaoming Hsu received his M.S. and Ph.D. degree in Electrical Engineering from The Pennsylvania State University, PA, in 1991 and 1995, respectively. He also received a M.S. degree in Engineering Management from National Tsing Hua University, Hsinchu, Taiwan in 2001. He has been worked for the National Space Organization (NSPO) of Taiwan on satellite flight software (Nov. 1995–Dec. 2000) and Loop Telecom on telecom-internet management software (Dec. 2000–July 2001). He was an associate professor in the National Formosa University (NFU) from July 2001–Jan. 2005. He is currently an associate professor and serves as the departmental chairperson in the Department of Electrical Engineering, National Chiayi University (NCYU), Chiayi City, Taiwan. His expertise is in machine learning, dynamic power management for embedded system, image processing, and pattern recognition.

Din Yuen Chan received his M.S. degree in medical engineering and his Ph.D. degree in electrical engineering from the Cheng Kung University in 1992 and 1996, respectively. He had been a senior engineer in Multi-Media Inc. to develop the videophone products. He was an associate professor at the Department of Information Engineering, I-Shou University from 1997 to 2003. Currently, he is the departmental chairperson and a professor in the department of Computer Science & Information Engineering, National Chiayi University (NCYU), Taiwan. He was the founder and served as chairperson of EE department at NCYU 2008–2011. He is also a member of the Technical Committee of VCIP and ISCAS. His research interests are in the areas of data compression, visual communication and image/video/audio signal processing.

Cheng-Ting Liu received his B.S. degree in Aeronautical Engineering from National Formosa University, Yunlin County, Taiwan, in 2005, and his M.S. degree in Computer Science and Information Engineering from National Chiayi University, Chiayi City, Taiwan, in 2008. He is currently working toward the Ph.D. degree at the department of Computer Science and Information Engineering, National Chiayi University. His research interests include artificial intelligence, embedded systems, and image processing.

Wei-Chieh Lai obtained his master degree in 2011 from the department of computer science and information engineering, National Chiayi University, Taiwan. His research interest is image processing and contour extraction.